Since January 2020 Elsevier has created a COVID-19 resource centre with free information in English and Mandarin on the novel coronavirus COVID-19. The COVID-19 resource centre is hosted on Elsevier Connect, the company's public news and information website.

Separation and Purification Technology 306 (2023) 122643

Contents lists available at ScienceDirect

Separation and Purification Technology

journal homepage: www.elsevier.com/locate/seppur

Turning waste into valuables: *In situ* deposition of polypyrrole on the obsolete mask for Cr(VI) removal and desalination

Fengkai Zhou [1], Yimeng Li [1], Shasha Wang, Xinkang Wu, Jiamin Peng, Fujun Wang, Lu Wang, Jifu Mao [*]

Key Laboratory of Textile Science & Technology, Ministry of Education, College of Textiles, Donghua University, Shanghai 201620, China
Key Laboratory of Textile Industry for Biomedical Textile Materials and Technology, Donghua University, Shanghai 201620, China

ARTICLE INFO

Keywords:
Mask recycling
Polypyrrole
Cr(VI) removal
Capacitive deionization

ABSTRACT

The global mask consumption has been exacerbated because of the coronavirus disease 2019 (COVID-19) pandemic. Simultaneously, the traditional mask disposal methods (incineration and landfill) have caused serious environmental pollution and waste of resources. Herein, a simple and green mass-production method has been proposed to recycle carbon protective mask (CPM) into the carbon protective mask/polydopamine/polypyrrole (CPM/PDA/PPy) composite by *in situ* polymerization of PPy. The CPM/PDA/PPy composite was used for the removal of Cr(VI) and salt ions to produce clean water. The synergistic effect of PPy and the CPM improved the removal capability of Cr(VI). The CPM/PDA/PPy composite provided high adsorption capacity (358.68 mg g^{-1}) and economic value (811.42 mg $\$^{-1}$). Consequently, the CPM/PDA/PPy (cathode) was combined with MnO_2 (anode) for desalination in CDI cells, demonstrated excellent desalination capacity (26.65 mg g^{-1}) and ultrafast salt adsorption rate (6.96 mg g^{-1} min^{-1}), which was higher than conventional CDI cells. Our work proposes a new low-carbon strategy to recycle discarded masks and demonstrates their utilization in Cr(VI) removal and seawater desalination.

1. Introduction

Wearing masks has become the most basic personal protection measure since the beginning of the coronavirus disease 2019 (COVID-19) pandemic [1]. Used masks were discarded indiscriminately and became a major source of plastic and toxic pollutants in the environment [2]. Discarded masks gradually generate microplastics upon degradation in the natural environment, which continue to accumulate in the food chain and cause great harm to the ecosystem [3]. Besides, discarded masks aggravate the issues of waste generation and inefficient use of resources [4]. Since most masks are single-use, they are discarded at an extremely high frequency (i.e., more than 130 billion masks are discarded globally every month) [5]. Additionally, common disposable face masks are made from nondegradable plastics, which take centuries to degrade in the environment [4,6]. Therefore, safe methods must be adopted to recycle discarded masks and eliminate their harm to the ecosystem and human health.

Various components in masks are difficult to separate and utilize, and the common treatment methods involve incineration or landfill [1,2,6]. However, these treatment methods waste resources and generate secondary pollution [7]. Discarded masks should also be converted into high-value-added products. Polypropylene (PP) is the main component of masks, and studies have shown that PP can be used as a material for the fabrication of carbon nanomaterials due to its high content of carbon (up to 85.7 wt%) [6]. To date, numerous studies have synthesized carbon nanomaterials from waste PP through catalytic carbonization. Wen et al. [8] successfully carbonized mixed polymers (PP/PE/PS) into CNTs using CB/Ni_2O_3 catalysts. Yang et al. [9] prepared CNTs by the catalytic pyrolysis of discarded masks using Ni–Fe bimetallic catalysts. Furthermore, Liu et al. [10] prepared carbon nanosheets from waste PP using a sulfur/ferrocene catalyst. Carbon nanomaterials prepared from discarded masks have been commonly used as electrode materials for supercapacitors and lithium-ion batteries [3], conductive nanofillers [11], and flame retardants [12]. However, in addition to the high cost of the catalyst, the catalyst must be removed from the product by acid treatment to improve the purity of the

* Corresponding author at: College of Textiles, Donghua University, 2999 North Renmin Road, Songjiang District, Shanghai 201620, China.
E-mail address: jifu.mao@dhu.edu.cn (J. Mao).
[1] These authors contributed equally to this article.

https://doi.org/10.1016/j.seppur.2022.122643
Received 30 August 2022; Received in revised form 27 October 2022; Accepted 9 November 2022
Available online 14 November 2022

synthesized carbon nanomaterials [6]. The purification process is time-consuming and creates additional environmental pollution. The handling of strong acids may lead to the destruction of the carbon skeleton [6]. Additionally, Li et al. [13] pyrolyzed PP into liquid fuels, producing energy from the plastic waste while mitigating mask pollution. However, the pyrolysis of PP often requires high temperatures and complicated processes [13]. The masks are not entirely composed of PP, and other organic and inorganic parts may also affect the pyrolysis behavior of PP [14]. Therefore, it is essential to provide a simple, safe, and low-cost strategy to recycle discarded masks, which brings higher economic benefits.

The water crisis has been exacerbated by accelerated urbanization, massive water pollution, misuse and lack of water management, forcing people to explore new ways to obtain cleaner and safer water [15]. Numerous studies have been conducted to obtain clean water by removing hexavalent chromium (Cr(VI)) from sewage or desalting seawater [16–24]. However, Cr(VI) exhibits high diffusibility and solubility in water and easily accumulates in the ocean, posing a threat to the marine ecosystem [16]. Therefore, removal of Cr(VI) and desalination are critical for obtaining safe and clean water. In this study, we prepared a carbon protective mask/polydopamine/polypyrrole (CPM/PDA/PPy) composite on the surface of CPM filters by *in situ* polymerization of PPy. The CPM/PDA/PPy composite production offers easy and safe synthesis, large-scale preparation, low cost (0.79 $ g^{-1}), and waste recycling. Using the CPM/PDA/PPy composite to remove Cr(VI) and salt ions to obtain clean water resources not only achieves the safe recycling of discarded masks (Fig. 1) but also conforms to the concept of "treatment of waste by waste". The CPM/PDA/PPy composite provides easy recovery and has an excellent removal capability for Cr(VI) (358.68 mg g^{-1} at 308 K) and desalination (26.65 mg g^{-1} at 1.2 V). Recycling masks provides two benefits: environmental restoration and the creation of high added value. This study provides a new low-carbon strategy for recycling discarded masks, which promises high application potential in clean water production.

2. Materials and methods

2.1. Materials

The CPM filters (which involve PP and activated carbon) have been sterilized by a vacuum ultraviolet lamp (ZW4D15Y-Z212, COMWIN, China) for 10 min after recycling. Pyrrole was acquired from Shanghai Macklin Biochemical Co., Ltd. Dopamine hydrochloride (DA, Sigma-H8502) was purchased from Sigma-Aldrich Trading Co., Ltd (Shanghai, China). Manganese dioxide (MnO_2, 98.8 %), carbon black (99.5 %), iron trichloride hexahydrate ($FeCl_3{\cdot}6H_2O$), ethanol absolute, N,N-dimethylformamide (DMF, ≥99.5 %), and tris(hydroxymethyl) aminomethane (≥99.5 %) were obtained from Sinopharm Chemical Reagent Co., Ltd (Shanghai, China). All chemicals were analytical reagents.

2.2. Fabrication of the CPM/PDA/PPy composite

The CPM/PDA/PPy composite was prepared via the *in situ* polymerization reaction (Fig. 2a). After adding 0.6 g of tris(hydroxymethyl) aminomethane and adjusting the pH to 8.5 to 100 mL of deionized water, 0.2 g of DA was added. The CPM was soaked in the solution for 8 h at ambient temperature. After being washed three times with deionized water, the CPM/PDA was dried at 50 °C for 6 h. Subsequently, the CPM/PDA was immersed in different concentrations of pyrrole (4–20 wt %) in 10 mL ethanol (absolute) and deionized water at ambient temperature for 1 h. Finally, $FeCl_3{\cdot}6H_2O$ (0.8 g) was dissolved in deionized water (10 mL) and added to the CPM/PDA/Py composites for 1 h. Under the action of oxidation, which initiated the polymerization reaction. Then, the CPM/PDA/PPy composite was washed three times with ultrapure water and dried at 60 °C for 6 h.

2.3. Characterization

The morphology of CPM/PDA/PPy composite was examined using scanning electron microscopy (SEM, Hitachi S-4800, Japan). Fourier-transform infrared (FT-IR) spectra of the as-prepared CPM/PDA/PPy composite before and after treatment were recorded on an FT-IR spectrophotometer (Perkin Elmer Spectrum Two, USA). The contact angle was determined using the captive droplet technique with a contact angle meter (Dataphysics OCA15EC, Germany). Using a strength tester (XQ-1C, Shanghai New Fiber Instrument Co., Ltd. China) to measured the tensile capabilities of the composite (a length of 4 cm and width of 1 cm). Before and after adsorption, the appearance of chemical contents of the CPM/PDA/PPy composite were examined using X-ray photoelectron spectroscopy (XPS, Thermofisher Escalab 250 xi, USA). Conductivity measurements were performed by a source meter unit (Keithley 2450, Tektronix, USA).

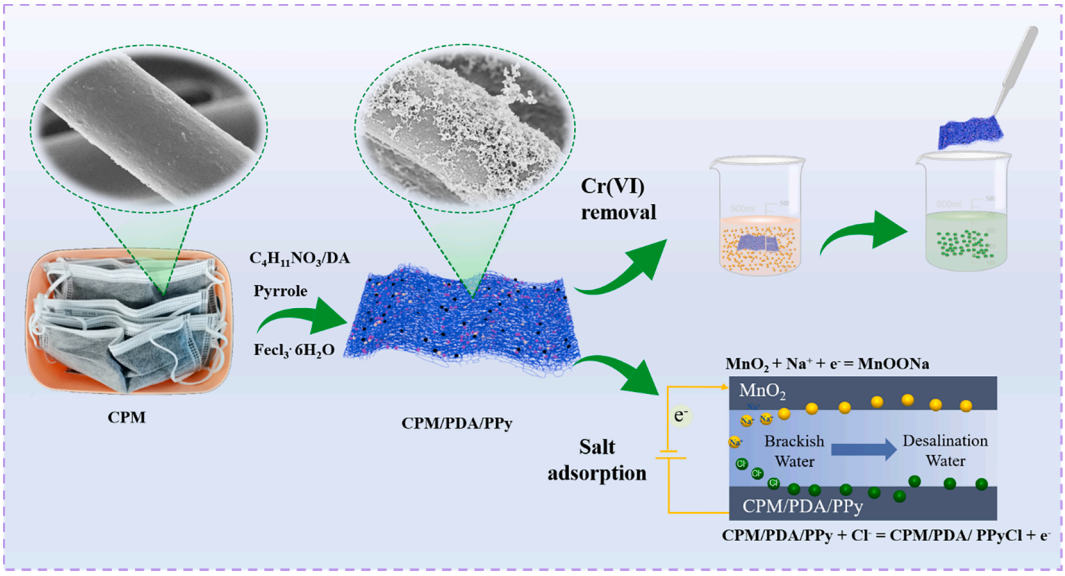

Fig. 1. Schematic of the use of CPM for Cr(VI) removal and desalination.

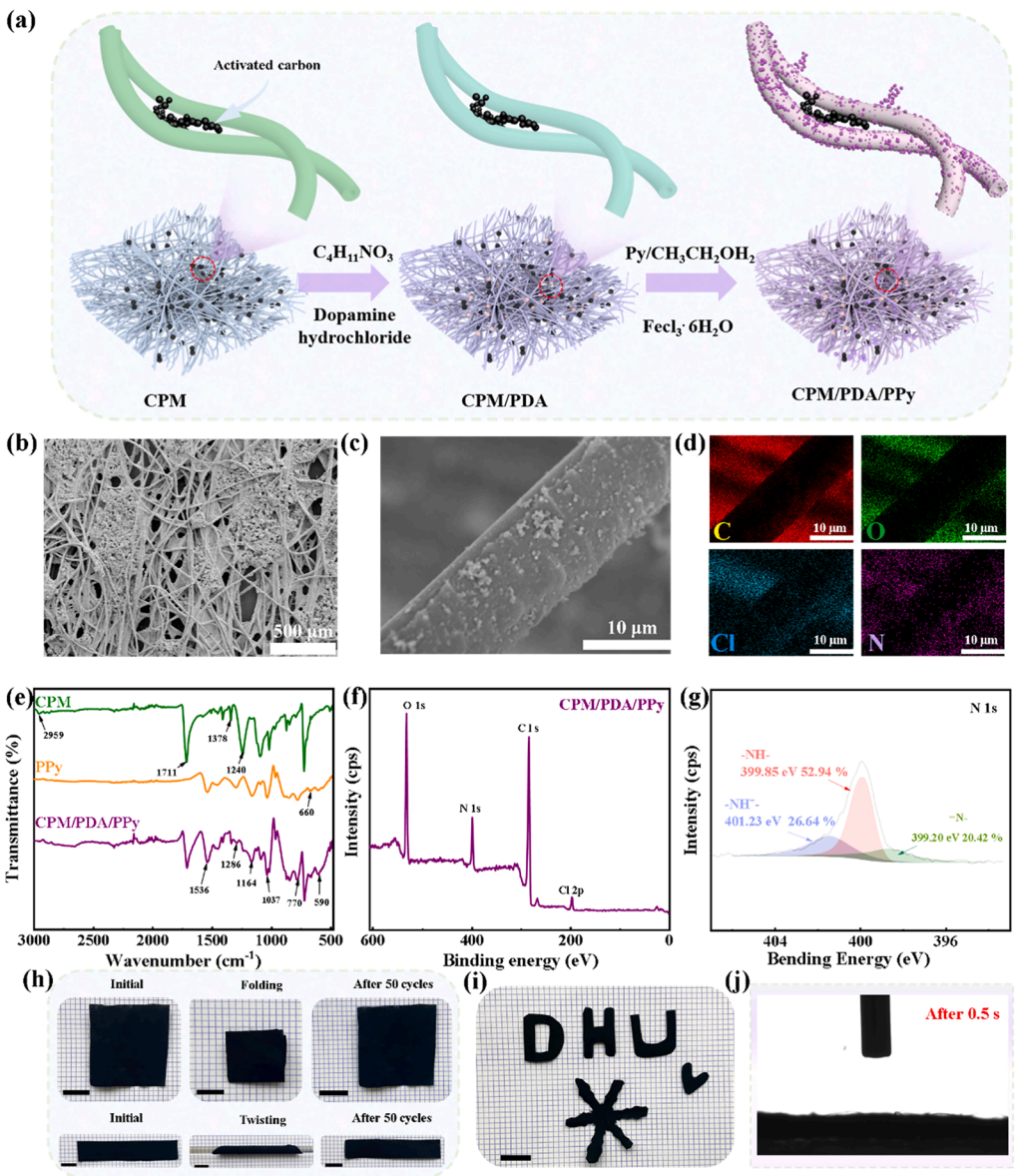

Fig. 2. Preparation of the CPM/PDA/PPy composite. (a) Scheme of the preparation of the CPM/PDA/PPy composite; SEM images of the CPM/PDA/PPy composite at (b) low and (c) high magnifications; (d) Elemental mapping of C, O, N, and Cl for the CPM/PDA/PPy composite; (e) FT-IR spectra of CPM, PPy, and the CPM/PDA/PPy composite; (f) XPS spectra of the CPM/PDA/PPy composite; (g) N1s XPS spectra of the CPM/PDA/PPy composite with high resolution; (h) Foldability and twistability testing, (i) Tailorability, and (j) Water wettability of the CPM/PDA/PPy composite. Scale bars were 2 cm in (h) and (i).

2.4. Cr(VI) removal

The CPM/PDA/PPy composite was used for batch adsorption experiments. 5 mg CPM/PDA/PPy composite was put in 5 mL Cr(VI) solution on a temperature-controlled shaker (60 rpm). The composite was extracted by tweezers, and the concentration of Cr(VI) in the solution after treatment was tested by a UV–visible spectrometer (X-6, Shanghai Metash Instruments Co., China). The Cr(VI) adsorption efficiency (% removal) and the adsorption capability at equilibrium (q_e) were calculated using Equations S1 and S2. Details including the pyrrole concentration, adsorbent mass, pH, kinetic experiments, adsorption isotherms, coexisting ions, and regeneration experiments can be found in Supporting Information.

2.5. CDI performance

The details of the preparation and electrochemical characterization of CPM/PDA/PPy electrodes are provided in Supporting Information. The CDI unit had a working surface of about 16 cm^2 and was made up of CPM/PDA/PPy and MnO_2 electrodes. A voltage of 1.2 V was used while 50 mL of the salt-containing solution (20 mL min^{-1}) was fed into the CDI unit. Then, it was circulated into a storage bottle. Real-time changes in brine concentration were measured using a conductivity probe connected to the CDI system. The details of the CDI performance of the CPM/PDA/PPy electrodes are offered in Supporting Information.

3. Results and discussion

3.1. Characterization of the CPM/PDA/PPy composite

The continuous filament PP fibers were randomly distributed to form a thin fiber web layer and there were many pores between the fiber webs, increasing the probability of contact with ions (Fig. S1a). The fiber surface was relatively smooth and flat,and activated carbon was mostly distributed in the fiber web in an aggregated state (Fig. S1b & c). Fig. 2b & c show the typical SEM images of the CPM/PDA/PPy composite. The structures of the fibers and activated carbon did not change, and PPy was successfully polymerized *in situ* on the surface of the fibers (Fig. 2b). The diameter of a single CPM/PDA/PPy fiber was about 15 μm, and PPy was evenly deposited on the surface of the CPM fiber (Fig. 2c). Further, C, O, N, and Cl were evenly distributed on the surface of the fibers according to energy dispersion spectroscopy (EDS) analysis (Fig. 2d). The

N and Cl peaks appeared in the full EDS spectrum of the CPM/PDA/PPy composite, further verifying the successful polymerization of PPy and the doping of Cl ions (Fig. S2).

The chemical structures CPM, PPy, and the CPM/PDA/PPy composite were characterized by FT-IR (Fig. 2e). The —CH_3 asymmetrical stretching vibration (2959 cm^{-1}) and bending vibration (1378 cm^{-1}) were the typical IR adsorption peaks of PP in CPM [25]. The C═O stretching vibrations (1711 cm^{-1}) and C—O stretching vibrations (1240 cm^{-1}) were the IR adsorption peaks of activated carbon in CPM [26,27]. The CPM/PDA/PPy composite exhibited typical PPy infrared absorption peaks. The peaks at 1536, 1286, 1164, and 1037 cm^{-1} corresponded to the pyrrole ring's C═C stretching, C—N stretching vibration, C—N in-plane deformation vibration, and C—H in-plane vibration, respectively [28]. The peaks at 770 and 660 cm^{-1} were correlated with the N—H wagging of PPy and the CPM/PDA/PPy composite [29]. Elements C, O, N, and Cl were seen in the XPS survey spectra of the CPM/PDA/PPy composite, demonstrating that the CPM/PDA/PPy composite was doped with Cl ions (Fig. 2f). Additionally, the N1s XPS spectra was deconvoluted into three peaks that correspond to ═N—, —NH—, and —NH^+— with binding energies of 399.20 eV, 399.85 eV, and 401.23 eV, respectively (Fig. 2g) [16]. These results confirmed that PPy was synthesized on the CPM by the *in situ* polymerization method.

Shape stability and mechanical strength must be considered to assess the viability of employing the CPM/PDA/PPy composite in water treatment. The mechanical characteristics of the composite are shown in Fig. S3. The extension at break values of the CPM and the CPM/PDA/PPy composite were 3.78 % and 3.41 %, and their breaking strengths were 11.75 N and 14.25 N, respectively, demonstrating that PDA and PPy coatings have negligible effects on the mechanical properties of the fiber mat. Moreover, CPM/PDA/PPy composite can quickly return to its original shape after folding and twisting in 50 repeated cycles (Fig. 2h). The weight of CPM/PDA/PPy composite was almost unchanged after 50 foldings and twistings, and the structure of the adsorbent remained intact and a large amount PPy remained coated on the surface of the fiber as seen by SEM (Fig. S4a–c). The CPM/PDA/PPy composite can be further processed and cut into different shapes for packaging or transportation (Fig. 2i). After PPy was formed on the CPM surface, composite from a contact angle of 112° (Fig. S5) to super hydrophilic, the droplets were quickly absorbed (0.5 s) by the CPM/PDA/PPy composite (Fig. 2j & MovieS1). It can be completely removed from deionized water by tweezers, put again, and quickly sunk to the bottom of the beaker, showing the flexibility and shape stability of the CPM/PDA/PPy composite (MovieS2). The CPM/PDA/PPy composite possesses excellent mechanical, flexible, and hydrophilic qualities that all helped with Cr (VI) adsorption in aqueous solutions.

3.2. Cr(VI) removal

3.2.1. Effects of the concentration of pyrrole, adsorbent dosage, and pH on Cr(VI) removal

One of the most crucial element influencing the adsorption action is the loading of PPy on the material. With the rise in the content of the pyrrole solution (0–20 wt%), the amount of PPy synthesized in the CPM gradually increased under $FeCl_3{\cdot}6H_2O$ oxidation, and the adsorption capacity for Cr(VI) enhanced from 20.9 % to 100 %. When the concentration of pyrrole was 12 wt%, the adsorption effect of Cr(VI) reached the best effect (Fig. S6a). In addition, the activated carbon in the CPM with a large specific surface area, and there were even finer pores and capillaries in the carbon particles, offering a strong adsorption capacity [30]. The increased loading of PPy was further demonstrated by the change in CPM/PDA/PPy conductivity at different pyrrole concentrations (Fig. S6b). After the pyrrole concentration reached 12 wt%, the Cr(VI) removal effect and the electrical conductivity did not change significantly. We selected the pyrrole concentration of 12 wt% to continue the experiment.

Controlling metal ion adsorption at the adsorbent site is largely up to the pH of the solution. For the CPM/PDA/PPy composite, the measured adsorption capacity dropped from 200 mg g^{-1} (pH = 2) to 8.3 mg g^{-1} (pH = 10) (Fig. 3a). The appearance characteristics of the adsorbent and the forms of Cr(VI)in the solution play major actions in Cr(VI) removal. The two main Cr(VI) species were $HCrO_4^-$ and $Cr_2O_7^{2-}$ when the pH was 2–6, while CrO_4^{2-} dominated when pH greater than 6 [28]. $HCrO_4^-$ is more easily adsorbed on the adsorbent than CrO_4^{2-} because it has the lowest adsorption energy and occupies the fewest adsorption sites [31]. As the pH increased, the deprotonation of – NH^+ groups caused a negative surface charge. In this case, the adsorption efficiency of the CPM/PDA/PPy composite decreased because of the competition between CrO_4^{2-} and OH^- on the adsorbent surface [32]. Consequently, the following adsorption tests proceeded at pH = 2. The removal efficiency of Cr(VI) was closed to 100 % when the CPM/PDA/PPy composite dosage reached 5 mg. Therefore, for further adsorption studies, 1 g L^{-1} was the best dosage (Fig. 3b).

3.2.2. Kinetic experiments and adsorption isotherms

The kinetic characteristics of the adsorption process of Cr(VI) were elucidated using the adsorption capability of the CPM/PDA/PPy composite at different adsorption times. Pseudo-first-order kinetics and pseudo-second-order kinetic models were used to analyze the kinetics of the Cr(VI) adsorption process, as given in Table S1. As the amount of time passed, the adsorption rate gradually decreased, and the adsorption capacity tended to stabilize (Fig. S7a). Because the higher starting concentration leads to more ions in contact with the material per unit of time, the larger adsorption driving force enhanced the adsorption capacity (Fig. S7b). The fitting curves of the pseudo-second-order models are given in Fig. S7a & c, and Table S2 are presented the kinetic parameters from the three kinetic models. The rate constant (k_2) obtained from the pseudo-second-order model diminished with the increase in the starting concentration, indicating that the adsorption took longer to achieve equilibrium. A higher correlation value (R^2 = 0.9986–0.9988) was shown in Table S2. These findings demonstrated that the process was mostly chemical adsorption and that the adsorption kinetics are well explained by the pseudo-second-order model. The kinetics data were subsequently examined using the intraparticle diffusion models to explore the adsorption process's diffusion mechanism and identify the rate-limiting stage [16]. Three distinct linear regions can be recognized on the curve, denoting the three adsorption stages of Cr(VI) (Fig. S7d). Since the Cr(VI) removal might be regulated by boundary layer diffusion, the mass of Cr(VI) was transferred from the solution to the appearance of the adsorbent in the first stage, which had the maximum slope and removal rate [33]. In the second stage, the adsorption rate gradually slowed, demonstrating that the rate-limiting mechanism at this stage was intraparticle diffusion [16]. The values of boundary layer thickness C_2 (2.8811–7.8693, Table S2) suggested that surface diffusion had an affected on the elimination of Cr(VI) as well [34]. As the decreased concentration of Cr(VI), the diffusion rate in the particles fell even further, ultimately achieving equilibrium.

The adsorption behavior of Cr(VI) at various temperatures (288 K, 298 K, and 308 K) was further studied. The Cr(VI) removal significantly enhanced with the temperature increased, demonstrating that the Cr(VI) removal process of the CPM/PDA/PPy composite was endothermic (Fig. 3c). We used the Langmuir model and the Freundlich model to fit the obtained test data to investigate the greatest adsorption capability and explore the adsorption reaction (Fig. 3c & Fig. S8a, b). The Langmuir and Freundlich isotherm models equations are listed in Table S3. The isotherm parameters (q_m, K_L, and K_F) all increased with the temperature (Table 1), also showing that the Cr(VI) removal was an endothermic reaction. In contrast, the Langmuir isotherm model can preferable explain the removal of Cr(VI) by the CPM/PDA/PPy composite because it has a greater R^2 value than the Freundlich model for all temperatures. The utmost adsorption capacity was enhanced from 92.08 mg g^{-1} to 358.68 mg g^{-1} when the temperature was raised from 288 K to 308 K (Table 1). Benefiting from the temperature rise, the

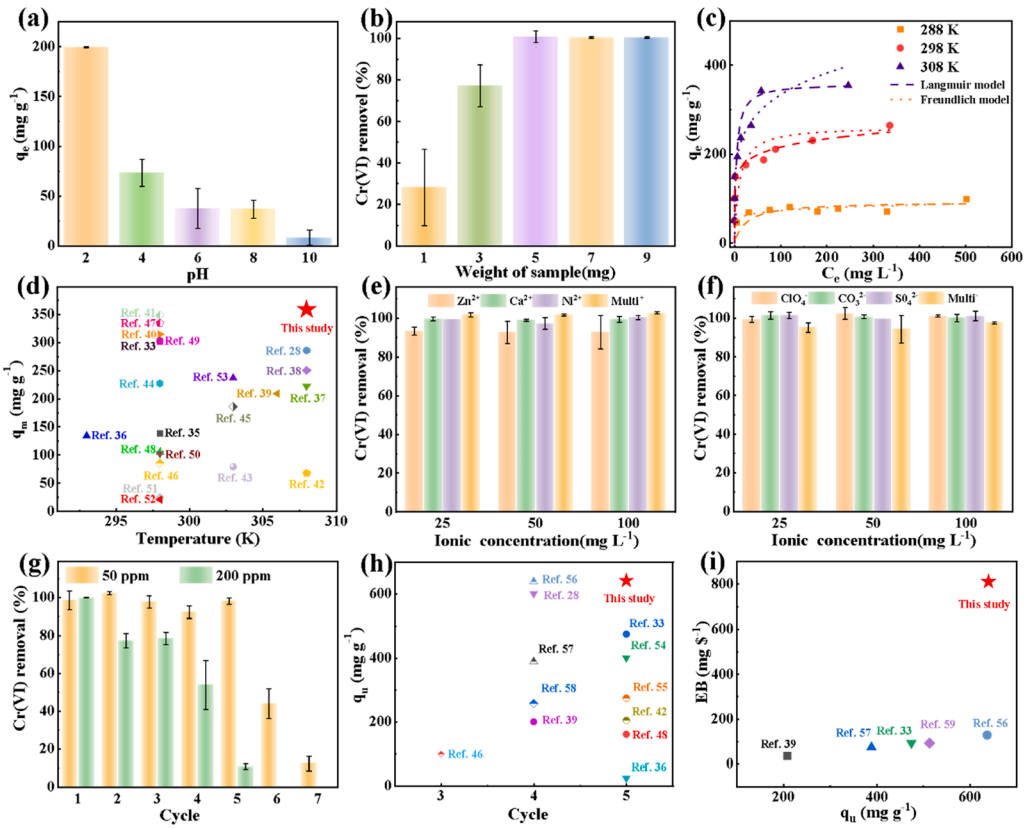

Fig. 3. Performance of the CPM/PDA/PPy composite in Cr(VI) removal. (a) Effect of solution pH on adsorption performance of Cr(VI); Adsorption of Cr(VI) with different masses of adsorbents (b) and temperatures (c); (d) Comparison of q_m of different materials; Effects of coexisting (e) cations and (f) anions on the adsorption of Cr(VI); (g) The adsorption–desorption cycles of Cr(VI) on the CPM/PDA/PPy composite; Comparison of (h) final adsorption capacity (q_u) and (i) economic benefits (EB) of different materials.

diffusion efficiency of Cr(VI) and the frequency of adsorbent contact were enhanced [16]. Thus, there was an increase in Cr(VI) adsorption on the adsorbent appearance. Fig. 3d and Table S4 summarize the adsorption performance comparison between the CPM/PDA/PPy composite and other materials, indicating that the CPM/PDA/PPy composite exhibited a relatively high removal capacity for Cr(VI) [28,33,35–53].

The thermodynamic parameters of Cr(VI) removal were computed using Equations S4 and S5 to investigate the thermodynamic characteristics of the adsorption reaction. The calculated thermodynamic parameters are shown in Table S5. Fig. S8c shows an upward trend when the temperature rose to 308 K from 288 K. At the set experimental temperature, the Gibbs free energy (ΔG°) values were all minus, demonstrating that the adsorption reaction of Cr(VI) was viable and spontaneous [28]. Moreover, the ΔG° value decreased as the temperature rose, illustrating the increase in spontaneity with the increased temperature [16].

3.2.3. *Practical applications and economic benefits*

Besides Cr(VI), plenty of other ions are also contained in sewage, which could challenge Cr(VI) for adsorption sites and reduce the elimination rate of Cr(VI) [28]. Fig. 3e presents the influence of Zn^{2+}, Ca^{2+}, Ni^{2+}, and $Multi^{+}$ (multiple cation ions) on Cr(VI) removal using the CPM/PDA/PPy composite. The Cr(VI) exhibited an adsorption efficiency that was much higher than 90 % demonstrating that coexisting cations would not affect Cr(VI) removal at 25 ppm, 50 ppm, and 100 ppm cation concentrations. Such as ClO_4^-, CO_3^{2-}, and SO_4^{2-} anions were negatively charged, they may contend with $HCrO_4^-$ for positively charged reaction sites on the CPM/PDA/PPy composite. As shown in Fig. 3f, at 25 ppm, 50 ppm, and 100 ppm coexisting cation concentrations, the elimination of Cr(VI) was almost 100 % effective, and the effect of coexisting anions was minimal [33]. The CPM/PDA/PPy composite has a remarkable potential for Cr(VI) removal from sewage.

The desorption of adsorbed metal ions is crucial for the reuse of adsorbents to maximize economic benefits. It has been reported that HCl can exude cationic Cr(III) from the adsorbent surface and release additional adsorption sites [36]. Therefore, 1 M HCl was used to treat the CPM/PDA/PPy composite to release Cr(VI) for further removal cycles. The recyclability of the CPM/PDA/PPy composite was tested using seven cycles of adsorption–desorption studies at a Cr(VI) concentration of 50 ppm (Fig. 3g). The CPM/PDA/PPy composite has a Cr(VI) adsorption efficiency of above 90 % in the first three cycles. However, during the sixth and seventh adsorption processes, the Cr(VI) removal capacity dropped to 44 % and 13.85 %, respectively. It may be that PPy was degraded during the adsorption–desorption process. Fig. S9a shows the Cr(VI) desorption efficiency of 1 M HCl. The use of HCl as a desorbent decreases the risk of secondary pollution and improves the material's ability to be recycled. The final adsorption capacity (q_u) of the adsorbent before failure was also an important parameter to evaluate its performance [16]. The Cr(VI) concentration of the actual process wastewater was greater than 100 ppm; thus, we increased the Cr(VI) concentration to 200 ppm and further explored q_u (Fig. 3g). Compared with the previously reported adsorbents [28,33,36,39,42,46,48,54–58], the CPM/PDA/PPy composite exhibited high ultimate adsorption capacity (641.02 mg g^{-1}, Fig. 3h). The CPM/PDA/PPy composite comprised a micron fiber mat that can be easily separated from the treated solution with little damage to the adsorbent. It can be seen that the CPM/PDA/PPy composite as a whole still maintains good integrity after five adsorption–desorption cycles (Fig. S9b). We find that the PPy coating on the fiber surface has fallen off through the high-magnification SEM, indicating that the PPy has degraded in multiple cycles, which may be the reason for the reduction of the adsorbent cycle effect (Fig. S9c). In addition to its strong adsorption capacity for Cr(VI), the cost of the adsorbent is an important concern that determines its mass production. The CPM/PDA/PPy composite exhibited extremely low cost and high economic efficiency (811.42 mg $\$^{-1}$, Fig. 3i and Table S6), which is higher than previously reported materials [33,39,56,57,59]. Since discarded masks are available everywhere, the mass production of the CPM/PDA/PPy composite using a simple reaction is feasible.

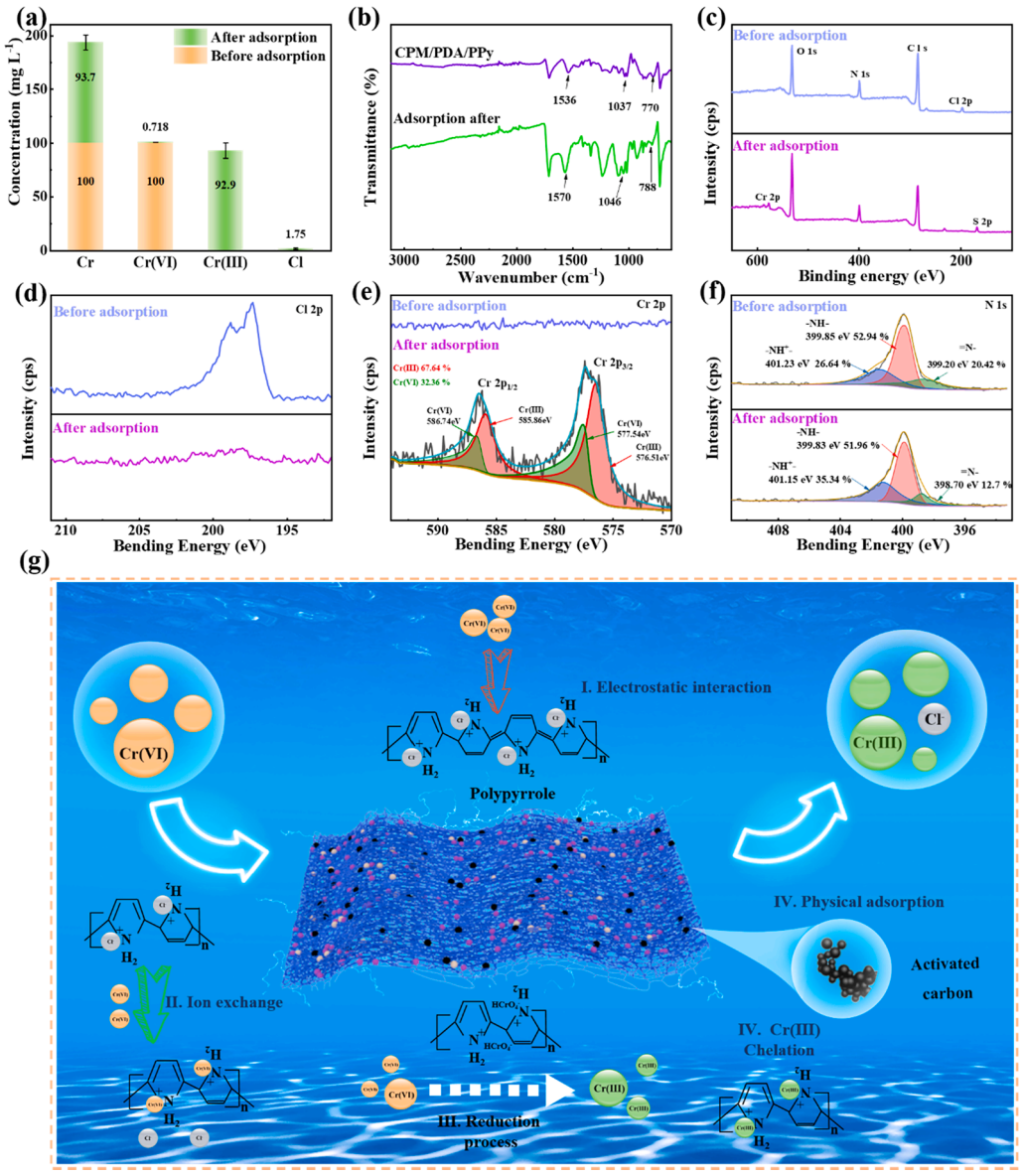

Fig. 4. Mechanism of Cr(VI) removal by CPM/PDA/PPy composite. (a) Various ion concentrations before and after the treatment of Cr(VI); (b) FT-IR spectra of the CPM/PDA/PPy composite following Cr(VI) adsorption; (c) XPS spectra of the CPM/PDA/PPy composite before and after Cr(VI) adsorption; High-resolution Cl 2p (d), Cr 2p (e), and N 1 s (f) XPS spectra of the CPM/PDA/PPy composite; (g) Schematic of the Cr(VI) removal mechanism via the CPM/PDA/PPy composite.

Table 1
Parameters of the adsorption isotherm model for Cr(VI).

Temperature (K)		288	298	308
Langmuir model	q_m (mg g^{-1})	92.08	262.33	358.68
	K_L(L mg^{-1})	0.0378	0.0967	0.2337
	R^2	0.9479	0.9896	0.9974
Freundlich model	1/n	0.1207	0.1208	0.1975
	K_F(mg L^{-1})	41.47	123.35	134.16
	R^2	0.7723	0.9319	0.9438

3.2.4. Cr(VI) removal mechanism

After the adsorption treatment, the total Cr ion content in the solution was 93.70 mg L^{-1}, the remaining Cr(VI) ion content was 0.72 mg L^{-1}, and the Cr(III) ion content was 92.90 mg L^{-1}, showing that Cr(VI) has been reduced to Cr(III) (Fig. 4a). Besides, the Cl^- ion content in the solution was tested. While there was no Cl^- ion in the solution before adsorption, the Cl^- ion concentration was 1.75 mg L^{-1} after adsorption treatment, probably due to the substitution between Cr ions and PPy [28]. By using FT-IR and XPS methods, the CPM/PDA/PPy composite before and after Cr(VI) removal were examined to reveal the mechanism of interaction of Cr(VI) on the adsorbent. Notably, the bands of the CPM/PDA/PPy composite shifted to higher values (1570 cm^{-1}, 1046 cm^{-1}, and 788 cm^{-1}) following adsorption of Cr(VI) (Fig. 4b). The existence of various species of Cr(VI) on CPM/PDA/PPy caused this shift, which destroyed the conjugated structure of PPy and constrained the degree of charge delocalization of the polymer chains [29].

Compared to the pristine sample, a new energy band appeared following Cr removal (Fig. 4c). The peak value of Cl 2p was considerably reduced following Cr(VI) adsorption (Fig. 4d), demonstrating the ion exchange happened. It has been reported that PPy to be highly protonated at low pH, and easier to triggered the ion exchange of Cl^- doped in PPy with oxyanions of Cr(VI) [38]. The Cr 2p peaks were divided into four peaks at 576.51 eV and 585.56 eV (Cr(III) $2p_{3/2}$ and Cr(III) $2p_{1/2}$), 577.54 eV and 586.74 eV (Cr(VI) $2p_{3/2}$ and Cr(VI) $2p_{1/2}$), demonstrating that Cr(VI) and Cr(III) coexisted on the CPM/PDA/PPy composite surface (Fig. 4e) [54]. Besides, the peak area of Cr(III) was 67.64 %, much more than the peak area of Cr(VI) 32.36 %. The existence of Cr(VI) on

the CPM/PDA/PPy composite surface can be attributed to the ion exchange and the electrostatic adsorption of Cr(VI) anions by PPy [16]. Additionally, Equations (1)–(3) explain the existence of Cr(III) on the CPM/PDA/PPy composite due to the reaction between Cr ions and PPy [28]:

$$HCrO_4^- + 3PPy^0 + 7H^+ \rightarrow Cr^{3+} + 4H_2O + 3PPy^+ \quad (1)$$

$$Cr_2O_7^{2-} + 6PPy^0 + 14H^+ \rightarrow 2Cr^{3+} + 7H_2O + 6PPy^+ \quad (2)$$

$$CrO_4^{2-} + 4H_2O + 3PPy^0 \rightarrow Cr^{3+} + 8OH^- + 3PPy^+ \quad (3)$$

where the reduction and oxidation states of PPy are represented by PPy^0 and PPy^+.

The N1s core-level spectra of CPM/PDA/PPy are shown in Fig. 4f. The ratio of the =NH— and —NH— groups peak areas in the adsorbent reduced after Cr(VI) adsorption from 20.42 % and 52.94 % to 12.7 % and 51.96 %, respectively. However, the percentage of the —NH^+— group was from 26.64 % up to 35.34 %. These results proved that Cr(VI) was bound, adsorbed, and reduced via the pyrrolic nitrogen groups on the adsorbent surface [35]. More significantly, the deprotonated pyrrole N can catch Cr(III) through the Cr(III)—N covalent bond and construct complexes [28].

Activated carbon in the CPM was favorable for Cr(VI) removal due to it containing extensive micropores and a high specific surface area, the CPM without PPy can also eliminate a part of Cr(VI) (Fig. S6a). The removal of Cr(VI) from the CPM/PDA/PPy composite can be characterized as a five-stage process based on the above explanation and the outcomes of the batch tests (Fig. 4g): (i) Through electrostatic interaction, Cr(VI) was adsorbed to the adsorbent by the positively charged nitrogen (N^+). (ii) The Cl^- ions doped on PPy undergo ion exchange with Cr(VI). (iii) Cr(VI) was reduced to Cr(III) by the state changes between PPy^0 and PPy^+. (iv) By forming Cr(III)—N covalent bonding, partly of Cr(III) was chelated on the deprotonated pyrrolic N. (v) Activated carbon enhanced the adsorption capacity of Cr(VI).

3.3. CDI performance

Capacitive deionization (CDI) is a potential desalination technique, because of it is low energy consumption and environmental friendliness, especially for the treatment of brackish water [21,60]. The CPM/PDA/PPy composite was used for the CDI electrode material. The capacitive performance of the electrode is a direct factor affecting the desalination capacity [22,61]. The measured electrochemical properties of the MnO_2 and CPM/PDA/PPy electrodes are displayed in Fig. S10. The cyclic voltammetry curves of the MnO_2 and CPM/PDA/PPy electrodes were an approximately rectangular shape, demonstrating that they acted as electric double layer capacitors (EDLC) (Fig. S10a & b, at a scan rate of 1–200 mV s^{-1}) [60]. The charge and discharge curves of MnO_2 and CPM/PDA/PPy electrodes were almost symmetrical (Fig. S10c & d, at an electric current density of 0.1–1 A g^{-1}), corroborating their EDLC behaviors. The specific capacitance (68.05F g^{-1}) was obtained for CPM/PDA/PPy at an electric current density of 0.1 A g^{-1} (Fig. S10e). The electrical resistance of the CPM/PDA/PPy electrodes was analyzed using electrochemical impedance spectroscopy, which showed a similar Nyquist curve, approximate straight line when it comes to low frequencies, but semicircle at high frequencies (Fig. S10f). This result indicated that the charge transfer resistance was lower and more conducive to the diffusion and transfer of ions [23,61].

The CDI performance of the CPM/PDA/PPy composite was investigated. The desalination capacities of the CPM/PDA/PPy electrodes were tested in a NaCl solution (700 mg L^{-1}; current velocity of 20 mL min^{-1}) with a cell voltage of 1.2 V. The schematic illustrations of the CDI units are shown in Fig. S11a. The temperature was maintained at 298 K during measurement using different concentrations of NaCl and measuring its conductivity, and the relationship between concentration (y) and conductivity (x) was obtained by y = 0.5307x − 76 (Fig. S11b). As shown in

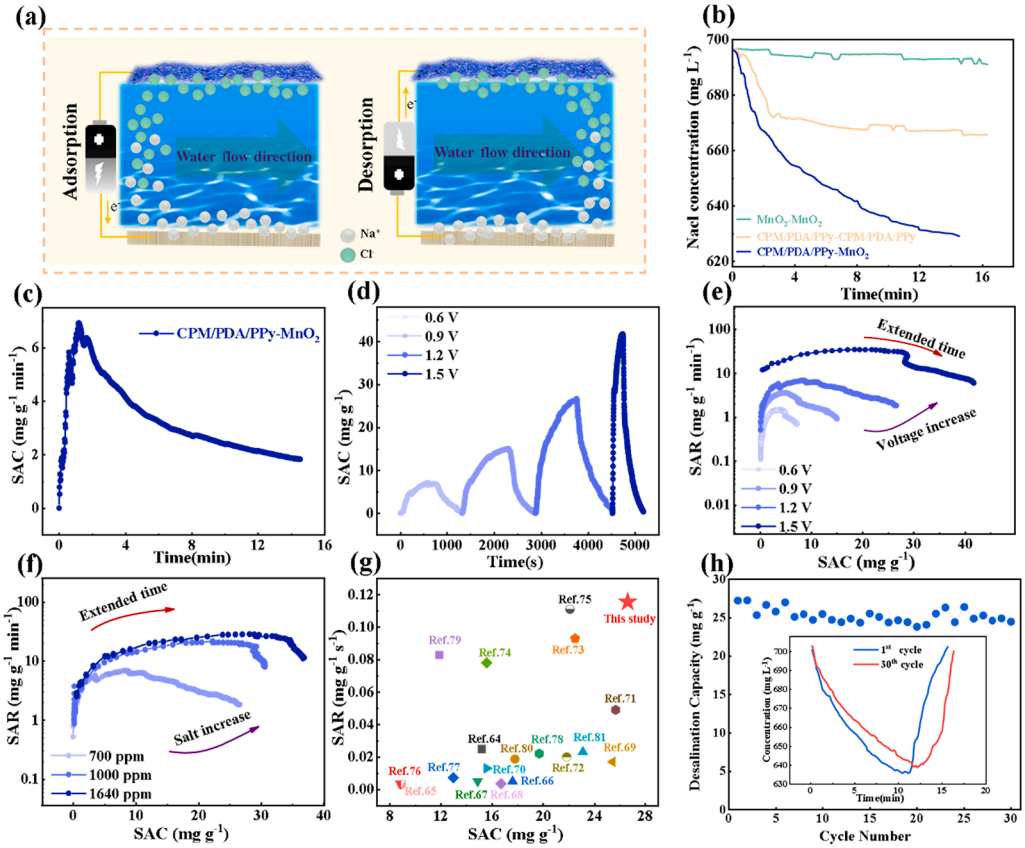

Fig. 5. CDI performance of CPM/PDA/PPy electrodes. (a) Schematic diagrams of the CDI adsorption and desorption of salts; (b) NaCl concentration variation over time; (c) Representative curves of the desalination rate at an applied cell voltage of 1.2 V; (d) Electrosorption–desorption cycles of CPM/PDA/PPy in NaCl solution sequentially at 0.6 V, 0.9 V, 1.2 V, and 1.5 V; Ragone plots of CPM/PDA/PPy in the above applied voltage (e) and different concentrations (f) of NaCl solutions; (g) Comparison of the SAR and SAC of CPM/PDA/PPy with other electrode materials; (h) Desalination cycling performance of CPM/PDA/PPy electrodes (the inset is the comparison of the desalination process in 1st cycle and 30th cycle).

Fig. 5a, after the voltage was applied, the counter ions entered the pores of the electrode and were saved in the electric double-layer capacitor [17]. Applying a reverse voltage caused the ions adsorbed on the electrode to be desorbed into the solution, so electrode recycling was realized by repeating the above process. The NaCl concentration dropped extremely, proving that Na^+ and Cl^- have been captured on the CPM/PDA/PPy electrode (Fig. 5b). And it can be found that when CPM/PDA/PPy (anode) was coupled with MnO_2 (cathode), the concentration of NaCl solution decreased the most, which may be due to the asymmetric configuration of the electrode to avoid the repulsion of co-ion [60].The solution concentration stabilized after 15 min, indicating that the deionization reached saturation. The desalination rate was another important parameter to evaluate the desalination performance, and the maximum desalination rate was found to be 6.96 mg g^{-1} min^{-1} (0.116 mg g^{-1} s^{-1}) at 1.2 V (Fig. 5c). Furthermore, the lesser internal resistance because of no ion exchange membrane and between the two electrodes distance was less than 3 mm, led to the faster desalination rate of our CPM/PDA/PPy cells. The reversible electrosorption–desorption cycling of CDI was observed (700 mg L^{-1}), and a typical voltage value was chosen between 0.6 V and 1.5 V (Fig. 5d). The CPM/PDA/PPy and MnO_2 electrodes were put into NaCl solution (700 mg L^{-1}) and a voltage of 1.5 V was applied, and the results showed that no obvious bubbles were generated on the surface of the electrodes after 30 min, proving that the applied voltage of ± 1.5 V would not caused severe water splitting (Fig. S12) [62]. Each electrosorption–desorption test was carried out at different voltages until the conductivity was almost constant. The electroabsorption capacity of salt ions was positively correlated with voltage, because of the stronger Coulomb interaction and enhanced electric double-layer capacitance performance [63]. When the conductivity was almost unchanged and the adsorption reached a steady state, the reverse voltage was applied by exchanging the positive and negative electrodes, and each electroabsorption–desorption process quickly and thoroughly released salt ions into the solution, further proving that the CPM/PDA/PPy electrode had good reversibility. By plotting the salt adsorption rate (SAR) and the salt adsorption capacity (SAC), as shown in Fig. 5e, the resulting Ragone plot showed that the desalination rate and capacity increased along with the heighten in operating voltage. The same phenomenon was observed when the salinity was changed (Fig. 5f). Higher salinity results in an increase in the ion transport flow inside CPM/PDA/PPy electrode, which enhances the electrosorption capacity [17]. The Ragone plot in Fig. 5f showed that higher salinity shifted the Ragone curve to the upper right region, demonstrating that higher salinity led to superior SAC and SAR. When the salinity was enhanced from 700 to 1640 mg L^{-1}, the electroabsorption capability was enhanced from 26.65 to 36.73 mg g^{-1}. Compared with the SAR and SAC of the reported materials [64–81], the CPM/PDA/PPy composite not only provided a better desalination ability but also had an excellent desalination rate (Fig. 5g). Additionally, the cost of electrode materials should be considered. Only low-cost and high-efficiency electrode materials can be used in the industry. Therefore, compared with other electrode materials (Table S7), the CPM/PDA/PPy composite provided better desalination ability at a lower cost (0.79 $ g^{-1}) compared to previously reported electrode materials [60,61,76,77,82,83]. This further highlights its advantages in brackish water desalination, increasing the added value of the CPM/PDA/PPy composite. The desalination cycle performance of the CPM/PDA/PPy–MnO_2 cell was tested for 30 cycles (Fig. 5h). It was worth noted that the highest desalination capacity reached 27.24 mg g^{-1}, and 89.88 % of the initial capacity was still maintained after 30 charge–discharge cycles, which proved that the electrode has superior long-term stability [84]. The 10.12 % desalination capacity reduction after 30 cycles is due to the following reasons: i) It can be observed that the size and structure of the electrode material remained in good integrity at the appearance (Fig. S13a-b). But the repeated intercalation and deintercalation of Na^+ and Cl^- ions will lead to the degradation of PPy after multiple charge-discharge cycles weakened the charge transfer ability of the electrode and reduced the desalination ability (Fig. S13c-d). ii)The side reactions (such as "anodic corrosion") will happened during the desalination process because the electrode was in direct contact with the solution, and the flow of the solution will also accelerated the corrosion of the electrode materials.

We recycled discarded masks and processed them with a simple PPy coating process to obtain the CPM/PDA/PPy composite. After adsorption of Cr(VI), the separation operation was simple, the adsorbent did not undergo cracking, any secondary pollution was avoided, and the regeneration performance was excellent. Under the synergistic effect of PPy and activated carbon, the CPM/PDA/PPy composite exhibited outstanding performance in Cr(VI) removal and desalination. Furthermore, the process was simple, low-cost, and easy to realize mass production, demonstrating applicability for providing access to safe and affordable water.

4. Conclusions

In summary, we prepared the CPM/PDA/PPy composite by *in situ* oxidative polymerization on discarded CPM, which was used for enhanced Cr(VI) removal and desalination. The CPM/PDA/PPy composite exhibited high Cr(VI) removal ability (358.68 mg g^{-1} at 308 K) and ultrahigh adsorption capacity (641.02 mg g^{-1}). In addition, CPM/PDA/PPy electrode was combined with MnO_2 electrode for brackish water treatment in CDI cells. The results demonstrated that the CPM/PDA/PPy–MnO_2 unit had an excellent salt removal capacity (26.65 mg g^{-1}) and a salt removal rate (max 6.96 mg g^{-1} min^{-1}) at 1.2 V, higher than conventional and membrane CDI cells. The CPM/PDA/PPy composite was extremely cost-effective in Cr(VI) removal (811.42 mg $\$^{-1}$). We believe that our work will play a role in discarded mask recycling and the alleviation of the drinking water crisis.

CRediT authorship contribution statement

Fengkai Zhou: Methodology, Formal analysis, Writing – original draft. **Yimeng Li:** Conceptualization, Validation, Visualization. **Shasha Wang:** Validation. **Xinkang Wu:** Validation. **Jiamin Peng:** Visualization. **Fujun Wang:** Resources. **Lu Wang:** Supervision. **Jifu Mao:** Writing – review & editing, Supervision, Project administration, Funding acquisition.

Declaration of Competing Interest

The authors declare that they have no known competing financial interests or personal relationships that could have appeared to influence the work reported in this paper.

Data availability

Data will be made available on request.

Acknowledgements

The authors acknowledge the support from the National Natural Science Foundation of China (Grant No.52005097), the Natural Science Foundation of Shanghai (Grant No.21ZR1401300), the Fundamental Research Funds for the Central Universities (2232022A-05), the 111 Project (Grant No. BP0719035), and the Fundamental Research Funds for DHU Distinguished Young Professor Program. The technical assistance of Jing Lin, Bingjun Rao, and Xiaoning Guan was greatly appreciated.

Appendix A. Supplementary material

Supplementary data to this article can be found online at https://doi.org/10.1016/j.seppur.2022.122643.

References

[1] S. Kim, X. Yang, K. Yang, H. Guo, M. Cho, Y.J. Kim, Y. Lee, Recycling respirator masks to a high-value product: From COVID-19 prevention to highly efficient battery separator, Chem. Eng. J. 430 (2022) 132723, https://doi.org/10.1016/j.cej.2021.132723.

[2] Z. Wang, C. An, X. Chen, K. Lee, B. Zhang, Q. Feng, Disposable masks release microplastics to the aqueous environment with exacerbation by natural weathering, J. Hazard. Mater. 417 (2021) 126036, https://doi.org/10.1016/j.jhazmat.2021.126036.

[3] J. Sreńscek-Nazzal, J. Serafin, A. Kamińska, A. Dymerska, E. Mijowska, B. Michalkiewicz, Waste-based nanoarchitectonics with face masks as valuable starting material for high-performance supercapacitors, J. Colloid Interface Sci. 627 (2022) 978–991, https://doi.org/10.1016/j.jcis.2022.07.098.

[4] L. Li, X. Zhao, Z. Li, K. Song, COVID-19: Performance study of microplastic inhalation risk posed by wearing masks, J. Hazard. Mater. 411 (2021), 124955, https://doi.org/10.1016/j.jhazmat.2020.124955.

[5] M. Saberian, J. Li, S. Kilmartin-Lynch, M. Boroujeni, Repurposing of COVID-19 single-use face masks for pavements base/subbase, Sci. Total Environ. 769 (2021) 145527, https://doi.org/10.1016/j.scitotenv.2021.145527.

[6] R. Yu, X. Wen, J. Liu, Y. Wang, X. Chen, K. Wenelska, E. Mijowska, T. Tang, A green and high-yield route to recycle waste masks into CNTs/Ni hybrids via catalytic carbonization and their application for superior microwave absorption, Appl. Catal., B 298 (2021), 120544, https://doi.org/10.1016/j.apcatb.2021.120544.

[7] C. Jehanno, J. Demarteau, D. Mantione, M.C. Arno, F. Ruipérez, J.L. Hedrick, A. P. Dove, H. Sardon, Selective Chemical Upcycling of Mixed Plastics Guided by a Thermally Stable Organocatalyst, Angew. Chem. Int. Ed. 60 (2021) 6710–6717, https://doi.org/10.1002/anie.202014860.

[8] X. Wen, X. Chen, N. Tian, J. Gong, J. Liu, M.H. Rümmeli, P.K. Chu, E. Mijiwska, T. Tang, Nanosized Carbon Black Combined with Ni2O3 as "Universal" Catalysts for Synergistically Catalyzing Carbonization of Polyolefin Wastes to Synthesize Carbon Nanotubes and Application for Supercapacitors, Environ. Sci. Technol. 48 (2014) 4048–4055, https://doi.org/10.1021/es404646e.

[9] W. Yang, L. Cao, W. Li, X. Du, Z. Lin, P. Zhang, Carbon Nanotube prepared by catalytic pyrolysis as the electrode for supercapacitors from polypropylene wasted face masks, Ionics 28 (7) (2022) 3489–3500, https://doi.org/10.1007/s11581-022-04567-7.

[10] X. Liu, C. Ma, Y. Wen, X. Chen, X. Zhao, T. Tang, R. Holze, E. Mijowska, Highly efficient conversion of waste plastic into thin carbon nanosheets for superior capacitive energy storage, Carbon 171 (2021) 819–828, https://doi.org/10.1016/j.carbon.2020.09.057.

[11] Z. Han, A. Fina, Thermal conductivity of carbon nanotubes and their polymer nanocomposites: A review, Prog. Polym. Sci. 36 (2011) 914–944, https://doi.org/10.1016/j.progpolymsci.2010.11.004.

[12] X. Wang, E.N. Kalali, J.-T. Wan, D.-Y. Wang, Carbon-family materials for flame retardant polymeric materials, Prog. Polym. Sci. 69 (2017) 22–46, https://doi.org/10.1016/j.progpolymsci.2017.02.001.

[13] C. Li, X. Yuan, Z. Sun, M. Suvarna, X. Hu, X. Wang, Y.S. Ok, Pyrolysis of waste surgical masks into liquid fuel and its life-cycle assessment, Bioresour. Technol. 346 (2022), 126582, https://doi.org/10.1016/j.biortech.2021.126582.

[14] G.K. Parku, F.-X. Collard, J.F. Görgens, Pyrolysis of waste polypropylene plastics for energy recovery: Influence of heating rate and vacuum conditions on composition of fuel product, Fuel Process. Technol. 209 (2020), 106522, https://doi.org/10.1016/j.fuproc.2020.106522.

[15] C. Zhang, L. Wu, J. Ma, M. Wang, J. Sun, T.D. Waite, Evaluation of long-term performance of a continuously operated flow-electrode CDI system for salt removal from brackish waters, Water Res. 173 (2020) 115580, https://doi.org/10.1016/j.watres.2020.115580.

[16] Y. Li, L. Lan, F. Zhou, J. Peng, L. Guo, F. Wang, Z. Zhang, L. Wang, J. Mao, Flexible and easy-handling pristine polypyrrole membranes with bayberry-like vesicle structure for enhanced Cr(VI) removal from aqueous solution, J. Hazard. Mater. 439 (2022), 129598, https://doi.org/10.1016/j.jhazmat.2022.129598.

[17] Y. Li, N. Chen, Z. Li, H. Shao, X. Sun, F. Liu, X. Liu, Q. Guo, L. Qu, Reborn Three-Dimensional Graphene with Ultrahigh Volumetric Desalination Capacity, Adv. Mater. 33 (2021) 2105853, https://doi.org/10.1002/adma.202105853.

[18] G. Bharath, A. Hai, T. Kiruthiga, K. Rambabu, M.A. Sabri, J. Park, M.Y. Choi, F. Banat, M.A. Haija, Fabrication of Ru–CoFe2O4/RGO hierarchical nanostructures for high-performance photoelectrodes to reduce hazards Cr(VI) into Cr(III) coupled with anodic oxidation of phenols, Chemosphere 299 (2022) 134439, https://doi.org/10.1016/j.chemosphere.2022.134439.

[19] G. Bharath, K. Rambabu, F. Banat, A. Hai, A.F. Arangadi, N. Ponpandian, Enhanced electrochemical performances of peanut shell derived activated carbon and its Fe3O4 nanocomposites for capacitive deionization of Cr(VI) ions, Sci. Total Environ. 691 (2019) 713–726, https://doi.org/10.1016/j.scitotenv.2019.07.069.

[20] G. Bharath, A. Hai, K. Rambabu, D. Savariraj, Y. Ibrahim, F. Banat, The fabrication of activated carbon and metal-carbide 2D framework-based asymmetric electrodes for the capacitive deionization of Cr(vi) ions toward industrial wastewater remediation, Environ. Sci. Water Res. Technol. 6 (2020) 351–361, https://doi.org/10.1039/C9EW00805E.

[21] K. Wang, Y. Liu, Z. Ding, Z. Chen, X. Xu, M. Wang, T. Lu, L. Pan, Chloride pre-intercalated CoFe-layered double hydroxide as chloride ion capturing electrode for capacitive deionization, Chem. Eng. J. 433 (2022) 133578, https://doi.org/10.1016/j.cej.2021.133578.

[22] K. Wang, L. Chen, G. Zhu, X. Xu, L. Wan, T. Lu, L. Pan, Ferroferric oxide@titanium carbide MXene heterostructure with enhanced sodium storage ability for efficient hybrid capacitive deionization, Desalination 522 (2022) 115420, https://doi.org/10.1016/j.desal.2021.115420.

[23] K. Wang, Y. Liu, Z. Ding, Z. Chen, G. Zhu, X. Xu, T. Lu, L. Pan, Controlled synthesis of NaTi2(PO4)3/Carbon composite derived from Metal-organic-frameworks as highly-efficient electrodes for hybrid capacitive deionization, Sep. Purif. Technol. 278 (2021) 119565, https://doi.org/10.1016/j.seppur.2021.119565.

[24] Z. Ding, X. Xu, J. Li, Y. Li, K. Wang, T. Lu, M.S.A. Hossain, M.A. Amin, S. Zhang, L. Pan, Y. Yamauchi, Nanoarchitectonics from 2D to 3D: MXenes-derived nitrogen-doped 3D nanofibrous architecture for extraordinarily-fast capacitive deionization, Chem. Eng. J. 430 (2022) 133161, https://doi.org/10.1016/j.cej.2021.133161.

[25] V.K. Thakur, D. Vennerberg, M.R. Kessler, Green Aqueous Surface Modification of Polypropylene for Novel Polymer Nanocomposites, ACS Appl. Mater. Interfaces 6 (12) (2014) 9349–9356, https://doi.org/10.1021/am501726d.

[26] J. Zawadzki, IR spectroscopic investigations of the mechanism of oxidation of carbonaceous films with HNO3 solution, Carbon 18 (1980) 281–285, https://doi.org/10.1016/0008-6223(80)90052-4.

[27] T.H. Usmani, T. Wahab Ahmed, S.Z. Ahmed, A.H.K. Yousufzai, Preparation and characterization of activated carbon from a low rank coal, Carbon 34 (1996) 77–82, https://doi.org/10.1016/0008-6223(95)00137-9.

[28] L.i. Xiang, C.-G. Niu, N. Tang, X.-X. Lv, H. Guo, Z.-W. Li, H.-Y. Liu, L.-S. Lin, Y.-Y. Yang, C. Liang, Polypyrrole coated molybdenum disulfide composites as adsorbent for enhanced removal of Cr(VI) in aqueous solutions by adsorption combined with reduction, Chem. Eng. J. 408 (2021) 127281, https://doi.org/10.1016/j.cej.2020.127281.

[29] Y. Shao, Z. Fan, M. Zhong, W. Xu, C. He, Z. Zhang, Polypyrrole/bacterial cellulose nanofiber composites for hexavalent chromium removal, Cellulose 28 (2021) 2229–2240, https://doi.org/10.1007/s10570-020-03660-2.

[30] L. Liao, W. Xiao, M. Zhao, X. Yu, H. Wang, Q. Wang, S. Chu, Y. Cui, Can N95 Respirators Be Reused after Disinfection? How Many Times? ACS Nano 14 (2020) 6348–6356, https://doi.org/10.1021/acsnano.0c03597.

[31] L. Zhang, F. Fu, B. Tang, Adsorption and redox conversion behaviors of Cr(VI) on goethite/carbon microspheres and akaganeite/carbon microspheres composites, Chem. Eng. J. 356 (2019) 151–160, https://doi.org/10.1016/j.cej.2018.08.224.

[32] Y. Zhan, S. He, X. Wan, J. Zhang, B. Liu, J. Wang, Z. Li, Easy-handling bamboo-like polypyrrole nanofibrous mats with high adsorption capacity for hexavalent chromium removal, J. Colloid Interface Sci. 529 (2018) 385–395, https://doi.org/10.1016/j.jcis.2018.06.033.

[33] N.H. Kera, M. Bhaumik, K. Pillay, S.S. Ray, A. Maity, Selective removal of toxic Cr (VI) from aqueous solution by adsorption combined with reduction at a magnetic nanocomposite surface, J. Colloid Interface Sci. 503 (2017) 214–228, https://doi.org/10.1016/j.jcis.2017.05.018.

[34] M.E. Argun, S. Dursun, C. Ozdemir, M. Karatas, Heavy metal adsorption by modified oak sawdust: Thermodynamics and kinetics, J. Hazard. Mater. 141 (2007) 77–85, https://doi.org/10.1016/j.jhazmat.2006.06.095.

[35] P. Karthikeyan, S.SD. Elanchezhiyan, S. Meenakshi, C.M. Park, Magnesium ferrite-reinforced polypyrrole hybrids as an effective adsorbent for the removal of toxic ions from aqueous solutions: Preparation, characterization, and adsorption experiments, J. Hazard. Mater. 408 (2021) 124892, https://doi.org/10.1016/j.jhazmat.2020.124892.

[36] W. Zhang, J.i. Ou, B. Wang, H. Wang, Q. He, J. Song, H. Zhang, M. Tang, L. Zhou, Y. Gao, S. Sun, Efficient heavy metal removal from water by alginate-based porous nanocomposite hydrogels: The enhanced removal mechanism and influencing factor insight, J. Hazard. Mater. 418 (2021) 126358, https://doi.org/10.1016/j.jhazmat.2021.126358.

[37] Z. Chen, K. Pan, Enhanced removal of Cr(VI) via in-situ synergistic reduction and fixation by polypyrrole/sugarcane bagasse composites, Chemosphere 272 (2021), 129606, https://doi.org/10.1016/j.chemosphere.2021.129606.

[38] Y. Li, Y. Gao, Q. Zhang, R. Wang, C. Li, J. Mao, L. Guo, F. Wang, Z. Zhang, L. Wang, Flexible and free-standing pristine polypyrrole membranes with a nanotube structure for repeatable Cr(VI) ion removal, Sep. Purif. Technol. 258 (2021) 117981, https://doi.org/10.1016/j.seppur.2020.117981.

[39] U.O. Aigbe, R. Das, W.H. Ho, V. Srinivasu, A. Maity, A novel method for removal of Cr(VI) using polypyrrole magnetic nanocomposite in the presence of unsteady magnetic fields, Sep. Purif. Technol. 194 (2018) 377–387, https://doi.org/10.1016/j.seppur.2017.11.057.

[40] JunKang Guo, L. Wang, YuLing Tu, H. Muhammad, XiaoHu Fan, G. Cao, M. Laipan, Polypyrrole modified bentonite nanocomposite and its application in high-efficiency removal of Cr(VI), J. Environ Chem. Eng. 9 (6) (2021) 106631, https://doi.org/10.1016/j.jece.2021.106631.

[41] W. Yao, T. Ni, S. Chen, H. Li, Y. Lu, Graphene/Fe3O4@polypyrrole nanocomposites as a synergistic adsorbent for Cr(VI) ion removal, Compos. Sci. Technol. 99 (2014) 15–22, https://doi.org/10.1016/j.compscitech.2014.05.007.

[42] J. Wang, K. Pan, Q. He, B. Cao, Polyacrylonitrile/polypyrrole core/shell nanofiber mat for the removal of hexavalent chromium from aqueous solution, J. Hazard. Mater. 244-245 (2013) 121–129, https://doi.org/10.1016/j.jhazmat.2012.11.020.

[43] R. Karthik, S. Meenakshi, Removal of hexavalent chromium ions from aqueous solution using chitosan/polypyrrole composite, Desalin. Water Treat. 56 (2015) 1587–1600, https://doi.org/10.1080/19443994.2014.951964.

[44] M. Bhaumik, A. Maity, V.V. Srinivasu, M.S. Onyango, Removal of hexavalent chromium from aqueous solution using polypyrrole-polyaniline nanofibers, Chem. Eng. J. 181-182 (2012) 323–333, https://doi.org/10.1016/j.cej.2011.11.088.

[45] A. Amalraj, M.K. Selvi, A. Rajeswari, E.J.S. Christy, A. Pius, Efficient removal of toxic hexavalent chromium from aqueous solution using threonine doped polypyrrole nanocomposite, J. Water Process Eng. 13 (2016) 88–99, https://doi.org/10.1016/j.jwpe.2016.08.013.

[46] J. Zhang, H. Chen, Z. Chen, J. He, W. Shi, D. Liu, H. Chi, F. Cui, W. Wang, Microstructured macroporous adsorbent composed of polypyrrole modified natural corncob-core sponge for Cr(vi) removal, RSC Adv. 6 (2016) 59292–59298, https://doi.org/10.1039/C6RA07687D.
[47] Y.Y. Tan, C. Wei, Y.Y. Gong, L.L. Du, Adsorption of hexavalent chromium onto sisal pulp/polypyrrole composites, IOP Conf. Ser.: Mater. Sci. Eng. 170 (2017) 012007, https://doi.org/10.1088/1757-899X/170/1/012007.
[48] N.S. Alsaiari, A. Amari, K.M. Katubi, F.M. Alzahrani, F.B. Rebah, M.A. Tahoon, Innovative Magnetite Based Polymeric Nanocomposite for Simultaneous Removal of Methyl Orange and Hexavalent Chromium from Water, Processes 9 (4) (2021) 576, https://doi.org/10.3390/pr9040576.
[49] J. Chen, X. Hong, Q. Xie, D. Li, Q. Zhang, Sepiolite Fiber Oriented-Polypyrrole Nanofibers for Efficient Chromium(VI) Removal from Aqueous Solution, J. Chem. Eng. Data 59 (7) (2014) 2275–2282, https://doi.org/10.1021/je500319a.
[50] H. Fan, H. Ren, X. Ma, S. Zhou, J. Huang, W. Jiao, G. Qi, Y. Liu, High-gravity continuous preparation of chitosan-stabilized nanoscale zero-valent iron towards Cr(VI) removal, Chem. Eng. J. 390 (2020) 124639, https://doi.org/10.1016/j.cej.2020.124639.
[51] C. Sakulthaew, C. Chokejaroenrat, A. Poapolathep, T. Satapanajaru, S. Poapolathep, Hexavalent chromium adsorption from aqueous solution using carbon nano-onions (CNOs), Chemosphere 184 (2017) 1168–1174, https://doi.org/10.1016/j.chemosphere.2017.06.094.
[52] S. Daradmare, M. Xia, V.N. Le, J. Kim, B.J. Park, Metal–organic frameworks/alginate composite beads as effective adsorbents for the removal of hexavalent chromium from aqueous solution, Chemosphere 270 (2021) 129487, https://doi.org/10.1016/j.chemosphere.2020.129487.
[53] K. Ding, X. Zhou, H. Hadiatullah, Y. Lu, G. Zhao, S. Jia, R. Zhang, Y. Yao, Removal performance and mechanisms of toxic hexavalent chromium (Cr(VI)) with ZnCl2 enhanced acidic vinegar residue biochar, J. Hazard. Mater. 420 (2021) 126551, https://doi.org/10.1016/j.jhazmat.2021.126551.
[54] Y. Xu, J. Chen, R. Chen, P. Yu, S. Guo, X. Wang, Adsorption and reduction of chromium(VI) from aqueous solution using polypyrrole/calcium rectorite composite adsorbent, Water Res. 160 (2019) 148–157, https://doi.org/10.1016/j.watres.2019.05.055.
[55] R. Guo, W. Guo, H. Pei, B. Wang, XuDong Guo, N. Liu, Z. Mo, Polypyrrole deposited electrospun PAN/PEI nanofiber membrane designed for high efficient adsorption of chromium ions (VI) in aqueous solution, Colloids Surf., A 627 (2021) 127183, https://doi.org/10.1016/j.colsurfa.2021.127183.
[56] N.H. Kera, M. Bhaumik, K. Pillay, S.S. Ray, A. Maity, Maity, m-Phenylenediamine-modified polypyrrole as an efficient adsorbent for removal of highly toxic hexavalent chromium in water, Mater. Today Commun. 15 (2018) 153–164, https://doi.org/10.1016/j.mtcomm.2018.02.033.
[57] N.H. Kera, M. Bhaumik, N. Ballav, K. Pillay, S.S. Ray, A. Maity, Selective removal of Cr(VI) from aqueous solution by polypyrrole/2,5-diaminobenzene sulfonic acid composite, J. Colloid Interface Sci. 476 (2016) 144–157, https://doi.org/10.1016/j.jcis.2016.05.011.
[58] A. Hosseinkhani, B. Forouzesh Rad, M. Baghdadi, Efficient removal of hexavalent chromium from electroplating wastewater using polypyrrole coated on cellulose sulfate fibers, J. Environ. Manage. 274 (2020) 111153, https://doi.org/10.1016/j.jenvman.2020.111153.
[59] A. Kong, Y. Sun, M. Peng, H. Gu, Y. Fu, J. Zhang, W. Li, Amino-functionalized MXenes for efficient removal of Cr(VI), Colloids Surf., A 617 (2021) 126388, https://doi.org/10.1016/j.colsurfa.2021.126388.
[60] G. Tan, S. Lu, N. Xu, D. Gao, X. Zhu, Pseudocapacitive Behaviors of Polypyrrole Grafted Activated Carbon and MnO2 Electrodes to Enable Fast and Efficient Membrane-Free Capacitive Deionization, Environ. Sci. Technol. 54 (2020) 5843–5852, https://doi.org/10.1021/acs.est.9b07182.
[61] S. Cao, T. Chen, S. Zheng, Y. Bai, H. Pang, High-Performance Capacitive Deionization and Killing Microorganism in Surface-Water by ZIF-9 Derived Carbon Composites, Small Methods 5 (2021) 2101070, https://doi.org/10.1002/smtd.202101070.
[62] Y. Tong, H. Liu, M. Dai, L.i. Xiao, X. Wu, Metal-organic framework derived Co3O4/PPy bifunctional electrocatalysts for efficient overall water splitting, Chin. Chem. Lett. 31 (9) (2020) 2295–2299, https://doi.org/10.1016/j.cclet.2020.03.029.
[63] C.-L. Yeh, H.-C. Hsi, K.-C. Li, C.-H. Hou, Improved performance in capacitive deionization of activated carbon electrodes with a tunable mesopore and micropore ratio, Desalination 367 (2015) 60–68, https://doi.org/10.1016/j.desal.2015.03.035.
[64] C. Tsouris, R. Mayes, J. Kiggans, K. Sharma, S. Yiacoumi, D. DePaoli, S. Dai, Mesoporous Carbon for Capacitive Deionization of Saline Water, Environ. Sci. Technol. 45 (23) (2011) 10243–10249, https://doi.org/10.1021/es201551e.
[65] Z.-H. Huang, M. Wang, L. Wang, F. Kang, Relation between the Charge Efficiency of Activated Carbon Fiber and Its Desalination Performance, Langmuir 28 (2012) 5079–5084, https://doi.org/10.1021/la204690s.
[66] Y. Liu, X. Xu, M. Wang, T. Lu, Z. Sun, L. Pan, Nitrogen-doped carbon nanorods with excellent capacitive deionization ability, J. Mater. Chem. A 3 (2015) 17304–17311, https://doi.org/10.1039/C5TA03663A.
[67] X. Xu, L. Pan, Y. Liu, T. Lu, Z. Sun, D.H.C. Chua, Facile synthesis of novel graphene sponge for high performance capacitive deionization, Sci. Rep. 5 (2015) 8458, https://doi.org/10.1038/srep08458.
[68] M. Ding, F.-H. Du, B. Liu, Z.Y. Leong, L. Guo, F. Chen, A. Baji, H.Y. Yang, Rod-like nitrogen-doped carbon hollow shells for enhanced capacitive deionization, FlatChem 7 (2018) 10–17, https://doi.org/10.1016/j.flatc.2018.01.002.
[69] C. Zhang, X. Wang, H. Wang, X. Wu, J. Shen, A positive-negative alternate adsorption effect for capacitive deionization in nano-porous carbon aerogel electrodes to enhance desalination capacity, Desalination 458 (2019) 45–53, https://doi.org/10.1016/j.desal.2019.01.023.
[70] J. Xie, J. Ma, L. Wu, M. Xu, W. Ni, Y.-m. Yan, Carbon nanotubes in-situ cross-linking the activated carbon electrode for high-performance capacitive deionization, Sep. Purif. Technol. 239 (2020) 116593, https://doi.org/10.1016/j.seppur.2020.116593.
[71] Y. Liu, B. Geng, Y. Zhang, X. Gao, X. Du, X. Dou, H. Zhu, X. Yuan, MnO2 decorated porous carbon derived from Enteromorpha prolifera as flow-through electrode for dual-mode capacitive deionization, Desalination 504 (2021) 114977, https://doi.org/10.1016/j.desal.2021.114977.
[72] A. Hai, B. Alqassem, G. Bharath, K. Rambabu, I. Othman, M. Abu Haija, F. Banat, Cobalt and nickel ferrites based capacitive deionization electrode materials for water desalination applications, Electrochim. Acta 363 (2020) 137083, https://doi.org/10.1016/j.electacta.2020.137083.
[73] F. He, A. Hemmatifar, M.Z. Bazant, T.A. Hatton, Selective adsorption of organic anions in a flow cell with asymmetric redox active electrodes, Water Res. 182 (2020) 115963, https://doi.org/10.1016/j.watres.2020.115963.
[74] H. Yoon, J. Lee, S. Kim, J. Yoon, Hybrid capacitive deionization with Ag coated carbon composite electrode, Desalination 422 (2017) 42–48, https://doi.org/10.1016/j.desal.2017.08.010.
[75] B.W. Byles, D.A. Cullen, K.L. More, E. Pomerantseva, Tunnel structured manganese oxide nanowires as redox active electrodes for hybrid capacitive deionization, Nano Energy 44 (2018) 476–488, https://doi.org/10.1016/j.nanoen.2017.12.015.
[76] F. Xing, T. Li, J. Li, H. Zhu, N. Wang, X. Cao, Chemically exfoliated MoS2 for capacitive deionization of saline water, Nano Energy 31 (2017) 590–595, https://doi.org/10.1016/j.nanoen.2016.12.012.
[77] P. Srimuk, F. Kaasik, B. Krüner, A. Tolosa, S. Fleischmann, N. Jäckel, M.C. Tekeli, M. Aslan, M.E. Suss, V. Presser, MXene as a novel intercalation-type pseudocapacitive cathode and anode for capacitive deionization, J. Mater. Chem. A 4 (2016) 18265–18271, https://doi.org/10.1039/C6TA07833H.
[78] H. Yoon, K. Jo, K.J. Kim, J. Yoon, Effects of characteristics of cation exchange membrane on desalination performance of membrane capacitive deionization, Desalination 458 (2019) 116–121, https://doi.org/10.1016/j.desal.2019.02.009.
[79] L. Agartan, K. Hantanasirisakul, S. Buczek, B. Akuzum, K.A. Mahmoud, B. Anasori, Y. Gogotsi, E.C. Kumbur, Influence of operating conditions on the desalination performance of a symmetric pre-conditioned Ti3C2Tx-MXene membrane capacitive deionization system, Desalination 477 (2020) 114627, https://doi.org/10.1016/j.desal.2019.114267.
[80] N. Liu, Y.i. Zhang, X. Xu, Y.i. Wang, A binder free hierarchical mixed capacitive deionization electrode based on a polyoxometalate and polypyrrole for brackish water desalination, Dalton Trans. 49 (19) (2020) 6321–6327, https://doi.org/10.1039/D0DT00162G.
[81] H. Liu, J. Zhang, X. Xu, Q. Wang, A Polyoxometalate-Based Binder-Free Capacitive Deionization Electrode for Highly Efficient Sea Water Desalination, Chem. – A Eur. J. 26 (19) (2020) 4403–4409, https://doi.org/10.1002/chem.201905606.
[82] F. Zhou, T. Gao, M. Luo, H. Li, Heterostructured graphene@Na4Ti9O20 nanotubes for asymmetrical capacitive deionization with ultrahigh desalination capacity, Chem. Eng. J. 343 (2018) 8–15, https://doi.org/10.1016/j.cej.2018.02.124.
[83] X. Yang, H. Jiang, W. Zhang, T. Liu, J. Bai, F. Guo, Y. Yang, Z. Wang, J. Zhang, A novel "butter-sandwich" Ti3C2Tx/PANI/PPY electrode with enhanced adsorption capacity and recyclability toward asymmetric capacitive deionization, Sep. Purif. Technol. 276 (2021) 119379, https://doi.org/10.1016/j.seppur.2021.119379.
[84] G. Bharath, N. Arora, A. Hai, F. Banat, D. Savariraj, H. Taher, R.V. Mangalaraja, Synthesis of hierarchical Mn3O4 nanowires on reduced graphene oxide nanoarchitecture as effective pseudocapacitive electrodes for capacitive desalination application, Electrochim. Acta 337 (2020) 135668, https://doi.org/10.1016/j.electacta.2020.135668.